ACCSCIENCE PUBLISHING

Materials Science in Additive Manufacturing

ORIGINAL RESEARCH ARTICLE

Computed tomography and finite element analysis-optimized Ti6Al4V bone plate combined with a porous 3D β-tricalcium phosphate cage for repairing segmental tibial defects in rabbits

Sung-Yen Lin[1,2,3,4,5†], Chih-Yun Lee[4,5,6†], Yen-Han Lai[4,5,7†], Wen-Fan Chen[5,8], Cheng-Tang Pan[5,9], Yu-Shun Cheng[9], Chung-Hwan Chen[3,4,5,8,10], and Chih-Kuang Wang[4,5,6,7,11*]

[1]School of Post-Baccalaureate Medicine, College of Medicine, Kaohsiung Medical University, Kaohsiung, Taiwan

[2]Department of Orthopedics, Kaohsiung Medical University Gangshan Hospital, Kaohsiung Medical University, Kaohsiung, Taiwan

[3]Department of Orthopedics, Kaohsiung Medical University Hospital, Kaohsiung Medical University, Kaohsiung, Taiwan

[4]Orthopaedic Research Center, Kaohsiung Medical University, Kaohsiung, Taiwan

[5]Regenerative Medicine and Cell Therapy Research Center, Kaohsiung Medical University, Kaohsiung, Taiwan

[6]PhD program in Life Sciences, College of Life Science, Kaohsiung Medical University, Kaohsiung, Taiwan

[7]Graduate Institute of Medicine, College of Medicine, Kaohsiung Medical University, Kaohsiung, Taiwan

[8]Institute of Medical Science and Technology, National Sun Yat-Sen University, Kaohsiung, Taiwan

[9]Department of Mechanical and Electromechanical Engineering, College of Engineering, National Sun Yat-sen University, Kaohsiung, Taiwan

[10]PhD Program in Biomedical Engineering, College of Medicine, Kaohsiung Medical University, Kaohsiung, Taiwan

[11]Department of Medicinal and Applied Chemistry, College of Life Science, Kaohsiung Medical University, Kaohsiung, Taiwan

[†]*These authors contributed equally to this work.*

***Corresponding author:**
Chih-Kuang Wang
(ckwang@kmu.edu.tw)

Citation: Lin S-Y, Lee C-Y, Lai Y-H, *et al*. Computed tomography and finite element analysis-optimized Ti6Al4V bone plate combined with a porous 3D β-tricalcium phosphate cage for repairing segmental tibial defects in rabbits. *Mater Sci Add Manuf*. 2026;5(3):026120019. doi: 10.36922/MSAM026120019

Received: March 19, 2026

Revised: April 21, 2026

Accepted: April 23, 2026

Published online: May 26, 2026

Abstract

Segmental bone defects caused by high-energy trauma remain a major clinical challenge because they often require mechanical stabilization and biological regeneration support for successful repair. Although autologous bone grafting is the clinical gold standard, its application is limited by donor-site morbidity and restricted graft availability. Metallic fixation devices provide mechanical stability, but metal-only implants do not actively support bone regeneration and may cause stress shielding or insufficient biological integration. To address these limitations, this study developed and evaluated two implant strategies for repairing rabbit tibial segmental defects. Computed tomography (CT) and computer-aided design (CAD) were used to establish a reproducible 5-mm rabbit tibial segmental defect model and guide implant design. Finite element analysis (FEA) optimized an integrated 3D-printed Ti6Al4V bone plate–cage construct with gradient porosity (50–70%) to reduce stress concentration while maintaining lightweight support. The cage construct

was evaluated alongside a hybrid system consisting of a 3D-printed Ti6Al4V bone plate paired with an interconnected porous 3D β-tricalcium phosphate (β-TCP) cage fabricated by digital light processing using a negative-temperature-responsive slurry. Owing to its interconnected porous architecture, relatively slow degradation profile, and compressive properties comparable to cancellous bone, the porous β-TCP cage provided favorable structural support and maintained defect-site stability during early-stage regeneration. At 90 days, *ex vivo* micro-CT and histological analyses in the hybrid group confirmed bone ingrowth, vascularization, and osteogenic tissue infiltration. Metal-induced imaging artifacts and histological sampling constraints in the Ti6Al4V cage construct limited direct comparison of regenerative outcomes between the two groups. These findings support the feasibility of combining essential early mechanical fixation with an osteoconductive porous β-TCP cage for segmental tibial defect repair.

Keywords: Segmental bone defects; Ti6Al4V; Bioceramic; Bone regeneration; Osteoconduction

1. Introduction

Segmental bone loss, often caused by high-energy trauma, remains a major clinical challenge because it frequently results in delayed union or non-union and often requires reconstructive surgery.[1] While small bone defects can usually be treated with bone grafting and fracture fixation, segmental defects often have poor spontaneous healing capacity and require more complex reconstruction to achieve stable repair and bone regeneration. Although multiple surgical approaches have been developed, clinical outcomes remain suboptimal.[1-3] Autografts are limited by donor-site morbidity and limited tissue availability, whereas allografts are constrained by immunological and biological incorporation issues.[4] Titanium implants can provide immediate mechanical stabilization, but when used alone, they do not actively support bone regeneration and may contribute to stress shielding or incomplete osseointegration.[5] Accordingly, new biomaterial strategies are still needed to enhance regeneration in segmental bone defects.

Optimal biomaterials for bone reconstruction must meet several criteria: satisfactory biocompatibility, mechanical properties like natural bone's elastic modulus, a degradation rate aligned with the bone healing process, and the ability to promote osteogenesis. While numerous biomaterials have been developed for craniofacial and long-bone defects, none fully meet the requirements of biocompatibility, strength, minimal morbidity, and effective osseointegration.[6,7] Among these, biocompatible metals, particularly titanium and its alloys, are preferred for load-bearing applications due to their superior toughness and strength.[8] Titanium scaffolds provide elasticity, high mechanical strength, and biocompatibility, supporting mineral deposition and cell proliferation without inducing inflammation or necrosis. However, their non-absorbable nature and high Young's modulus (>110 GPa) compared to bone tissue (7–30 GPa) often render them unsuitable as standalone solutions, as they can cause stress shielding, implant loosening, and failure.[9,10]

Conversely, bioceramics offer promising bioactivity, biodegradability, and biocompatibility, making them viable candidates for bone reconstruction.[11] Traditional porous bioceramic scaffolds, fabricated via methods such as gas foaming, salt leaching, freeze-drying, or polymer templating, suffer from low mechanical strength, poor reproducibility, and limited control over internal features (e.g., pore size, shape, and interconnectivity) and over the overall scaffold geometry.[12] Additive manufacturing has revolutionized bioceramic scaffold production by enabling layer-by-layer construction with precise pore structures. Our group has developed a novel negative thermo-responsive bioceramic slurry ink system based on poly(N-isopropylacrylamide) (pNIPPAm), which facilitates the creation of 3D bioceramics using robotic extrusion deposition and digital light processing (DLP).[12,13] This system leverages the shrinkage of pNIPPAm's intramolecular hydrogen bonds above 32–35 °C to uniformly drain the water of the slurry, thereby tightly packing ceramic powders.[12-14] After sintering at 1,150–1,250 °C, the resulting mechanically stable 3D bioceramic scaffolds exhibit a dense structural skeleton with well-defined, interconnected porosity, enhancing bone regeneration. Despite these advances, bioceramics remain inherently brittle, and highly porous scaffolds lack the mechanical stability required for repairing trauma-induced segmental bone defects, underscoring the need

for biomaterials that promote osteogenesis while reducing reliance on autogenous bone.

However, each biomaterial presents unique advantages and limitations. Given the complex composition of bone tissue and the dynamic nature of bone remodeling, no single material can universally address all regeneration scenarios.[15] A promising strategy to meet these clinical demands involves combining a metal bone plate with robust mechanical fixation and a bioactive interconnected porous 3D bioceramic scaffold for guided bone regeneration to address segmental long-bone loss.

We hypothesized that a mechano-biologically optimized 3D-printed Ti6Al4V bone plate combined with a mechanically stable, interconnected porous 3D bioceramic cage would provide sufficient fixation stability to prevent implant-related failure while promoting bone ingrowth and osseointegration within the scaffold. A 5-mm rabbit tibial segmental defect was selected as a suitable and reproducible model for evaluating early-stage bone regeneration and treatment efficacy, while minimizing the risks of non-union and fixation failure that are more commonly encountered in larger rabbit segmental defect models. To test this hypothesis, our study adopted two complementary strategies. First, computed tomography (CT) and computer-aided design (CAD) were used to reconstruct a 3D tibial model of the New Zealand rabbit, followed by finite element analysis (FEA) in ANSYS Workbench under defined boundary conditions. Building on our previous work, we designed an integrated 3D-printed Ti6Al4V plate–cage construct with gradient porosity (50–70%) to reduce stress concentration while maintaining lightweight mechanical support.[16] Second, the optimized 3D Ti6Al4V bone plate was paired with a matching interconnected porous 3D bioceramic cage with osteoconductive characteristics and compressive properties comparable to cancellous bone, thereby enhancing early fixation and structural stability during defect repair. Because standalone fixation using 3D Ti6Al4V bone plate was unsuccessful in preliminary animal studies, two configurations—an integrated Ti6Al4V plate with a gradient-porous Ti6Al4V cage and a Ti6Al4V plate combined with a mechanically stable porous 3D bioceramic cage—were evaluated *in vivo* for surgical stability, osseointegration, and bone regeneration. This strategy may also have translational relevance for high tibial osteotomy, in which current grafting approaches remain associated with complications and variable long-term success rates ranging from 40% to 85%.[17] Figure 1 provides a graphical overview of this research, aiming to achieve robust bone integration and regeneration in segmental tibial defects in New Zealand rabbits.

2. Materials and methods

2.1. Preparation of 3D Ti6Al4V bone plate with a gradient-porous cage

The FEA-optimized design of the 3D Ti6Al4V bone plate with a gradient-porous cage scaffold for repairing rabbit tibial defects was adapted from our previous report.[16] The FEA section used the following material properties: cortical bone, E = 17 GPa, ν = 0.3; cancellous bone, E = 5 GPa, ν = 0.2; bone marrow, E = 3.0×10^{-7} GPa, ν = 0.45; Ti-6Al-4V, E = 110 GPa, ν = 0.31; and hydroxyapatite (Hap), E = 10 GPa, ν = 0.3. This design effectively reduces excessive stiffness and mitigates stress shielding effects. A brief description of the design process follows: Adult New Zealand White rabbit models were constructed and meshed to accurately simulate natural bone structure. The left tibia was selected as the target site, and a 5-mm segmental defect was designed in the mid-diaphysis. To ensure high fidelity in FEA, CT scans (Ingenuity 128 CT, Philips, Netherlands) were performed and imported into InVesalius 3.1 software (CTI Renato Archer, Brazil) in Digital Imaging and Communications in Medicine (DICOM) format. Cortical and cancellous bones were modelled separately based on CT data. Following the determination of the prosthesis shape, fixation pattern, and 1:1 scale modeling, FEA was conducted. Stress distribution was simulated under physiologically relevant loading conditions.

An optimal 3D Ti6Al4V bone plate with a cage scaffold featuring a gradient porosity of 70%, 65%, 60%, 55%, and 50% was designed. Both the standard 3D Ti6Al4V bone plate and the gradient-porous variant were fabricated via selective laser melting, yielding excellent structural integrity and fine pores on the scaffold surface. The bone plates underwent annealing to enhance stability, making them suitable for future clinical applications in tibial defect repair. The FEA confirmed that the gradient-porous design achieves uniform force distribution, closely mimicking natural bone mechanics, and is expected to minimize stiffness-related damage and stress shielding. These constructs were subsequently evaluated *in vivo* to assess fixation stability and bone regeneration. Figure 2 illustrates the 3D digital models and physical objects of the optimal 3D Ti6Al4V bone plate (Figure 2A) and the gradient-porous variant (Figure 2B).

2.2. Fabrication of interconnected porous 3D bioceramic cages using digital light processing

2.2.1 Materials

The 3D-printed interconnected porous bioceramic cage scaffold was fabricated using the raw materials and methods outlined in our previous study.[16] The bioceramic powder comprised 70% β-tricalcium phosphate (β-TCP) (Sigma-

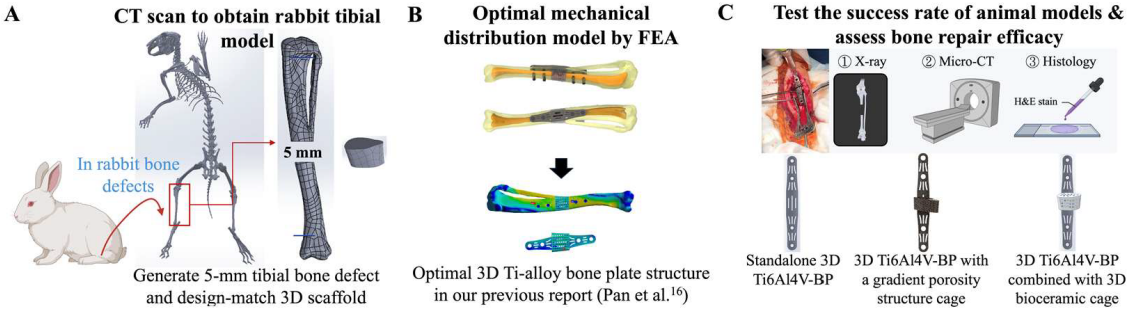

Figure 1. Graphical overview of the study. (A) Computed tomography (CT) scans of adult New Zealand White rabbits are used to generate a 3D skeletal model of the tibia, which is converted to an editable STP file for computer-aided design (CAD) software. A 5-mm segmental defect is designed in the mid-tibial shaft as the target site. (B) An optimal 3D-printed Ti6Al4V bone plate (3D Ti6Al4V-BP) with a gradient-porous Ti6Al4V cage is developed based on stress distribution analysis of the natural rabbit tibia from our previous study.[16] (C) Two configurations are evaluated *in vivo* using a rabbit tibial segmental defect model: the 3D Ti6Al4V-BP with a gradient-porous Ti6Al4V cage, and the 3D Ti6Al4V-BP paired with an interconnected porous bioceramic cage mimicking natural spongy bone. Outcomes assessed include surgical feasibility, fixation stability, and osseointegration.
Abbreviation: FEA: Finite element analysis.

Aldrich, United States of America [USA]) and 30% HAp (CAPTALS®, Plasma Biotal Limited, United Kingdom). The photocurable slurry included this bioceramic powder mixed with ethanol, trimethylolpropane triacrylate (TMPTA) (Sigma-Aldrich), NIPPAm (a negative thermo-responsive monomer; Tokyo Chemical Industry Co., Ltd., Japan), phenylbis(2,4,6-trimethylbenzoyl)phosphine oxide (a photoinitiator; Irgacure® 819, I819, Tokyo Chemical Industry Co., Ltd., Japan), and poly(ethylene glycol) diacrylate (PEGDA, 700 Da; VIEW STAR CO., LTD, Taiwan). All chemicals were used as received.

2.2.2 Design and fabrication of interconnected porous 3D bioceramic cages

Although integrated 3D Ti6Al4V plate–cage fixation constructs can provide early mechanical stabilization of bone defects, their long-term use may still be associated with stress shielding, screw loosening, soft-tissue irritation, and infection. In our preliminary trial, the 3D Ti6Al4V plate was used alone without any interbody scaffold. The 5-mm segmental defect was left unfilled, requiring the plate–screw construct to bear all axial, bending, and torsional loads during ambulation. As observed in our pilot experience, rabbits typically resumed spontaneous standing and weight-bearing within 48 hours postoperatively, generating continuous cyclic loading across the unsupported gap. The resulting micromotion at the screw–bone interface prevented osseointegration and led to progressive screw loosening, followed by plate fracture at the mid-plate stress concentration zone. This mechanical failure confirmed that a plate-only bridging construct is insufficient for stabilizing a segmental tibial defect in a rabbit model. Therefore, a hybrid design consisting of an FEA-optimized 3D Ti6Al4V bone plate and a 3D-printed interconnected porous bioceramic cage was adopted to stabilize the defect, promote early osseointegration, and support restoration of structural continuity and functional load transfer following bone regeneration (Figure 2B). Literature suggests that an optimal pore size for bioceramic bone graft materials ranges from 100 to 1,000 μm.[18] Based on 1:1 CT modeling, a cage-shaped scaffold with interconnected pore channels was designed to match the 5-mm segmental defect in the rabbit tibial shaft (Figure 3A). The optimized 3D Ti6Al4V bone plate was tailored to the outer surface of the tibia and paired with the interconnected porous bioceramic cage with rounded corners to enhance surgical fit, structural stability, and osteoconductive bone ingrowth.

The interconnected porous 3D β-TCP cages and standard compression cylinder samples were fabricated using a top-down DLP 3D printer (Octave Light R1, Octave Light Ltd., Hong Kong). Based on preliminary process optimization, the printing parameters were set at a UV wavelength of 405 nm, an exposure time per layer of 5 s, a layer thickness of 50 μm, and a 35% vol. photocurable ceramic slurry composed of β-TCP/HAp (70/30) powder dispersed in an ethanol-based NIPPAm/PEGDA/TMPTA system. A standard stereolithography (STL) file generated from a 3D CAD model created in Tinkercad® (Autodesk Inc., USA) was imported into the printer. After printing, the green bodies were washed with water and cleaned by ultrasonication to remove uncured slurry. The printed bodies were then immersed in water for 10 min to replace residual ethanol and facilitate thermally induced shrinkage of the pNIPPAm network during subsequent heating. Silicone oil (polydimethylsiloxane, Sigma-Aldrich) was applied to improve uniform water release

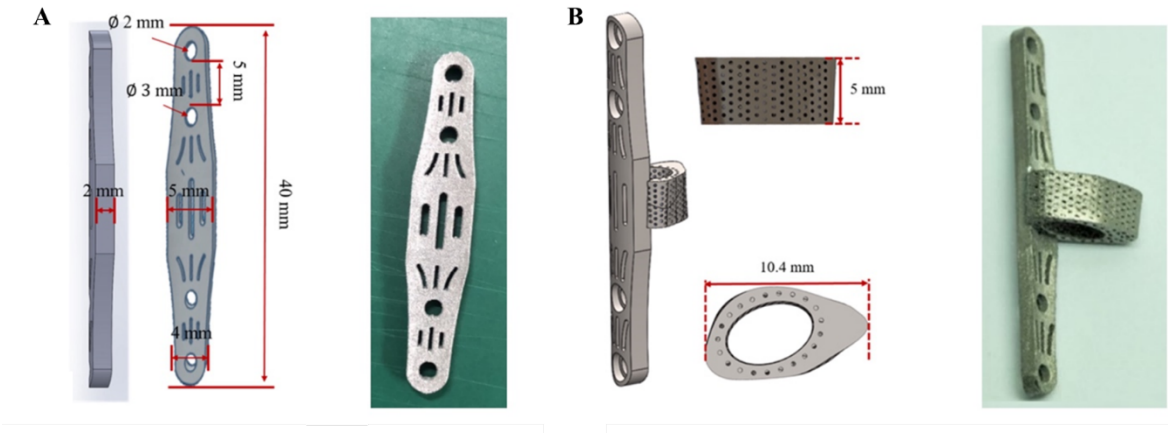

Figure 2. Finite element analysis (FEA)-guided design of optimized Ti6Al4V bone plate constructs based on screw and rabbit tibial models.[16] (A) Representative digital models and printed constructs of the 3D-printed Ti6Al4V bone plate (3D Ti6Al4V-BP). (B) Integrated 3D Ti6Al4V-BP with a gradient-porous Ti6Al4V cage.

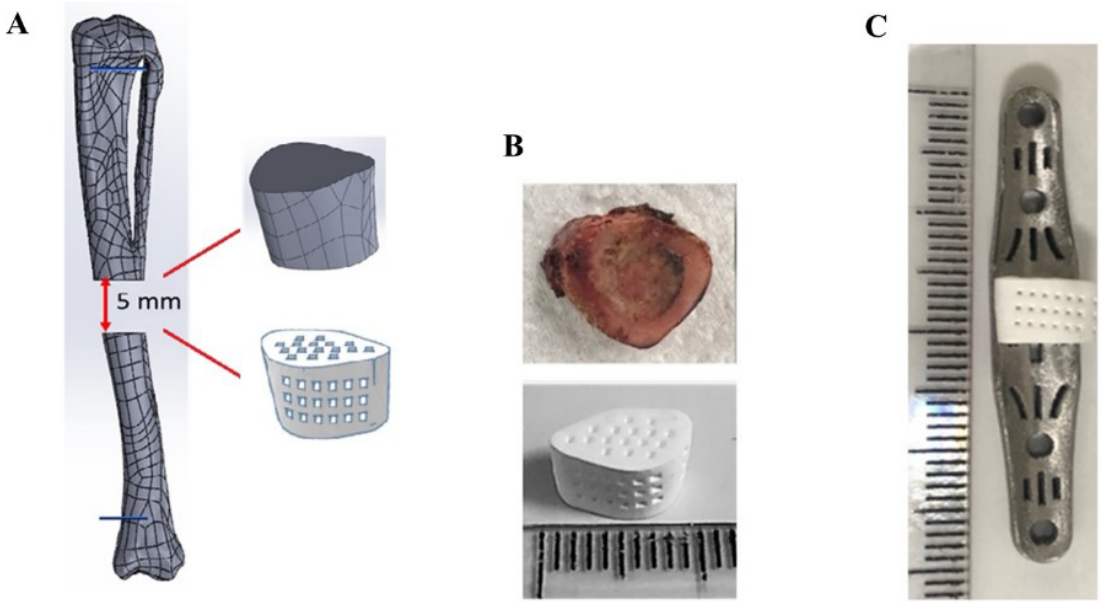

Figure 3. Interconnected porous bioceramic cage for tibial reconstruction. (A) The stereolithography (STL) image of the cage-shaped scaffold with interconnected pore-channel geometry is designed to match a 5-mm segmental defect in the mid-diaphysis of the rabbit tibia. (B) The overall appearance of the resected rabbit tibial specimen and the digital light processing-fabricated interconnected porous 3D bioceramic cage. (C) The interconnected porous 3D bioceramic cage with rounded corners is designed to fit securely into the optimized 3D Ti6Al4V bone plate.

and particle packing during drying. The green bodies were dried at 60 °C for 1–3 h, de-binding at 500–600 °C, and sintered at 1,150 °C for 2 h in a muffle furnace (LH 15/14, Nabertherm, Germany), resulting in densified scaffold struts with interconnected pore channels and enhanced mechanical integrity (Figure 3B). After sintering, the predominant crystalline phase was confirmed to be β-TCP. The sintered compression β-TCP samples exhibited a compressive strength of 11.38 ± 1.72 MPa, calculated using the external dimensions of cylindrical specimens (φ 4.8 × 12.0 mm). Additional physicochemical characterization and cytocompatibility data have been reported in our previous study.[13] The sintered β-TCP cage, designed with rounded corners, was then fitted into the Ti6Al4V bone plate to improve defect conformity, structural stability, and osteoconductive bone ingrowth (Figure 3C).

2.2.3. X-ray diffraction analysis

The crystalline phases of the samples were characterized using X-ray diffraction (XRD) analysis (Bruker D2-Phaser,

Bruker, Germany). Measurements were performed with Cu-Kα radiation operating at an accelerating voltage of 30 kV and a current of 10 mA. The diffraction patterns were collected over a 2θ range of 20° to 40° at a scanning rate of 2°/min. Prior to analysis, all samples were dried and ground into fine powders to ensure homogeneity. Phase identification was conducted by comparing the obtained diffraction peaks with reference data from the International Centre for Diffraction Data (ICDD) database.

2.2.4. Scanning electron microscopy evaluation

The surface morphology and microstructural characteristics of the samples were examined using scanning electron microscopy (SEM; JEOL JSM-6330TF, JEOL, Japan). Prior to imaging, all specimens were dried and mounted on specimen stubs using carbon tape, followed by sputter-coating with a thin layer of gold (Au) to enhance conductivity. SEM observations were performed at an accelerating voltage of 5 kV under high-vacuum conditions. Images were acquired at various magnifications to evaluate surface topology and pore structure.

2.3. Animal experiments

2.3.1. Establishment of tibial segmental defects in rabbits

This study should be regarded as a pilot investigation designed to provide preliminary evidence of surgical feasibility and early biological response. In adherence to the 3Rs framework governing ethical animal research, particularly the principle of reduction, the sample size (n = 3 per group) was deliberately minimized to avoid unnecessary use of experimental subjects at this early stage of implant development. Consequently, formal inferential statistics were not applied, and the results should be interpreted as exploratory rather than confirmatory. The preliminary findings nonetheless provide proof-of-concept data to inform the design of a future study incorporating a priori power analysis, an expanded cohort, and appropriate statistical rigor.

All animal procedures were approved by the Institutional Animal Care and Use Committee of Kaohsiung Medical University (KMU), Taiwan (Approval No. 108196). New Zealand White rabbits were housed at the KMU Animal Research Center, and all experimental procedures were performed in accordance with institutional ethical guidelines to minimize animal pain and discomfort. Six 12–13-week-old rabbits were randomly assigned to two experimental groups (n = 3 per group). All animals were male and were allocated to experimental groups by simple randomization using a random number draw prior to surgery. We acknowledge that blinding of outcome assessors during histological analysis was not feasible in this study, as the two scaffold types were readily distinguishable by their material appearance, rendering complete group concealment during tissue assessment impossible.

All surgical procedures were performed under general anesthesia induced by intramuscular (IM) injection of ketamine (40 mg/kg) and xylazine (10 mg/kg). Prophylactic antibiotics (amikacin, 5 mg/kg, IM) were administered prior to surgery. Under sterile conditions, the left tibia was shaved, disinfected, and surgically exposed through a longitudinal incision along the medial aspect. A 5-mm segment of the mid-tibial shaft was removed to create a segmental bone defect. The cut bone ends were trimmed, and the defect site was irrigated with 30 mL of normal saline. Postoperative analgesia was provided by IM injection of ketorolac (1 mg/kg) for three days following surgery, in conjunction with continued antibiotic administration (amikacin, 5 mg/kg, IM) and wound care.

Two implant configurations were evaluated, both using the optimized 3D-printed Ti6Al4V bone plate for fixation: (i) an integrated Ti6Al4V plate with a gradient-porous Ti6Al4V cage, and (ii) a Ti6Al4V bone plate paired with an interconnected porous 3D bioceramic cage. These groups were assessed *in vivo* for surgical feasibility, fixation stability, osseointegration, and bone regeneration in the rabbit tibial defect model. The experimental design, surgical procedure, and study timeline are illustrated in Figure S1.

2.3.2. Soft X-ray radiograph analysis

Postoperative soft X-ray radiography was performed to confirm implant positioning and defect alignment using an X-ray machine (M-100, SOFTEX, Japan) operated at 70 kVp, 2 mA, a 44 cm source-to-film distance, and a 1.5 s exposure time. *In vivo* radiographic examinations were conducted immediately after surgery and again before sacrifice to monitor construct stability and gross bone healing within the defect region.

2.3.3. Micro-computed tomography evaluation

In vivo micro-CT was performed at designated postoperative time points in anesthetized rabbits using a Skyscan 1076 system (Bruker, Belgium), and the reconstructed images were analyzed with CTAn software (1.23.02+). Scanning parameters included a 0.5-mm aluminum filter, an isotropic resolution of 9 or 35 μm, an X-ray voltage of 50 kV, a current of 200 μA, and an exposure time of 600 ms. The region of interest extended from the proximal tibia across the defect site to the distal tibia. The total volume (TV, mm^3) corresponded to the 5-mm defect region. New bone volume (BV, mm^3) was

quantified by grayscale thresholding, in which mineralized tissues within grayscale values of 10–40 were segmented; the lower threshold included both scaffold and newly formed bone, whereas the higher threshold represented the scaffold phase alone. Accordingly, BV was calculated by subtracting scaffold volume from the total mineralized volume and was then normalized to TV for each rabbit.

2.3.4. Histological evaluation

At 90 days after implantation, the rabbits were euthanized for histological evaluation. Harvested tibial specimens were fixed in 10% neutral buffered formalin (KINGFEX CO., LTD., Taiwan) for 48 h, decalcified in 14% ethylenediaminetetraacetic acid (EDTA; Sigma-Aldrich) prepared in phosphate-buffered saline (PBS; Gibco, USA) for 28 days, and embedded in paraffin (Epredia, USA). Longitudinal and coronal sections (5-μm thick) were prepared using a microtome (Leica RM2255 Fully Automated Rotary, Leica, Germany) and stained with hematoxylin and eosin (H&E; Sigma-Aldrich) for qualitative histological assessment and histomorphometric analysis. Digital images were analyzed using Image-Pro Plus 5.0 software (Media Cybernetics, Inc., USA). At 40× magnification, the callus area within 1 mm proximal and distal to the implant ends, as well as the intact cortical bone area of the native tibia, was measured for quantitative comparison.

3. Results and discussion

3.1. Microstructure, shrinkage behavior, porosity, and density of the interconnected porous 3D β-tricalcium phosphate cage

X-ray diffraction analysis (Figure S2) confirmed that the predominant crystalline phase of the sintered interconnected 3D porous bioceramic cage was β-TCP. SEM images (Figure 4) further revealed the characteristic microstructure of the DLP-fabricated β-TCP cage at multiple magnifications. At low magnification, the scaffold exhibited a well-defined square pore-channel architecture with pore sizes ranging from 500 to 800 μm (Figure 4A), which falls within the range considered favorable for bone regeneration, cell infiltration, and vascularization.[18,19] The regular pore geometry also demonstrated the geometric fidelity achievable by DLP-based fabrication. At 100× magnification (Figure 4B), the scaffold showed a layered structure with an interlayer spacing of approximately 50–70 μm, consistent with the layer-by-layer photocuring process. This microscale surface topography may contribute to cell attachment and tissue ingrowth.[20] At higher magnifications (1,000× [Figure 4C] and 2,000× [Figure 4D]), the scaffold struts displayed a densely sintered granular morphology with grain sizes of approximately 0.5–5 μm. Such multiscale surface roughness and grain packing are characteristic of sintered calcium phosphate ceramics and may enhance both surface bioactivity and mechanical integrity.[21-23]

The dimensional changes of the scaffold during drying and sintering are summarized in Table 1. After drying at 60 °C, the scaffold exhibited shrinkage of 10.2 ± 0.4% in the X–Y direction and 5.2 ± 0.6% in the Z direction, without visible cracking. Following sintering, the shrinkage increased to 7.5 ± 0.2% in the X–Y direction and 10.6 ± 0.4% in the Z direction, resulting in total shrinkage values of 17.7% and 15.8%, respectively. The anisotropic shrinkage behavior is consistent with previous reports on DLP-printed ceramics and can be attributed to directional differences in interlayer particle packing, mesoscale porosity, and sintering-driven densification along the printing axis.[24-26] These findings highlight the importance of compensating for dimensional shrinkage during CAD design and optimizing slurry composition and printing parameters to improve dimensional accuracy after sintering.

Table 1. The results of average shrinkage, average bulk density, average apparent density, and total porosity of the sintered interconnected porous 3D bioceramic cage

Parameter	Value
Shrinkage ratio (%)	
Drying	
X–Y direction	10.2 ± 0.4
Z direction	5.2 ± 0.6
Sintered	
X–Y direction	7.53 ± 0.2
Z direction	10.6 ± 0.4
Density (g/cm^3)	
Bulk	1.31 ± 0.40
Apparent	2.93 ± 0.15
Total porosity (%)	55.3

As shown in Table 1, the scaffold exhibited a bulk density of 1.31 ± 0.4 g/cm^3 and an apparent density of 2.93 ± 0.15 g/cm^3. The apparent density approached the theoretical density of β-TCP (3.14 g/cm^3), indicating a high degree of densification in the solid phase,[27] whereas the lower bulk density reflected the intentionally preserved open

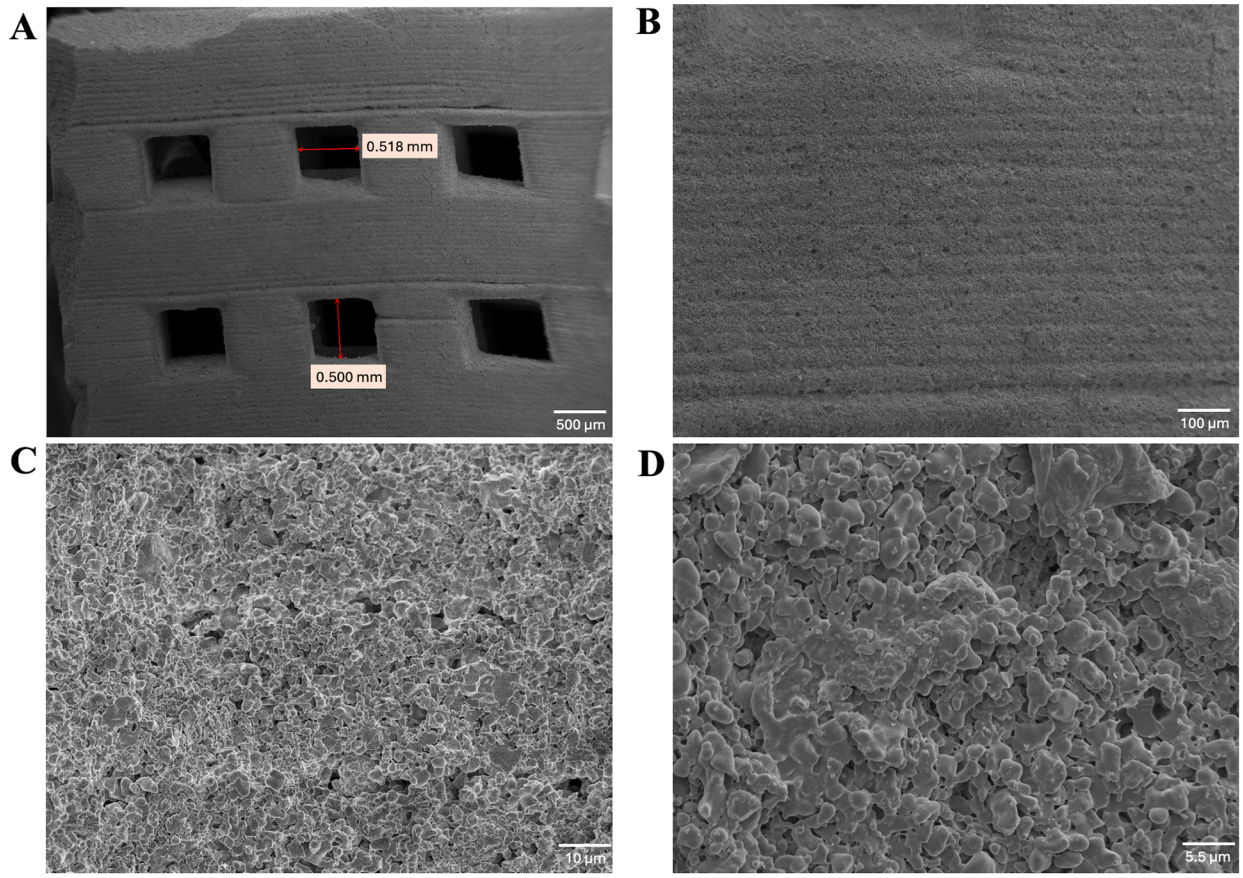

Figure 4. A scanning electron microscope images the side view of a sintered interconnected porous 3D bioceramic cage at varying magnifications. (A) A macro-view of the sample with defined square pore channel features at 25× magnification (scale bar: 500 µm). (B) Surface morphology at 100× magnification with defined layer thickness (scale bar: 100 µm). (C–D) Higher-magnification views (C: 1,000×, scale bar: 10 µm; D: 2,000×, scale bar: 5.5 µm) reveal the detailed granular structure, size, and degree of densification.

porous architecture. The scaffold porosity was estimated using bulk density and apparent density according to Equation 1, and was 55.3%, which falls within the range generally considered suitable for bone tissue engineering and supports cell infiltration, nutrient transport, and vascular invasion. Together with the apparent density (95.4% of theoretical) and compressive strength (11.38 ± 1.72 MPa),[13] these results indicate that the interconnected porous 3D β-TCP cage achieved a favorable balance between structural stability and biological permeability. Such properties are particularly important in this study, as the cage was intended not only to maintain the defect space but also to provide an osteoconductive framework for subsequent bone regeneration. Although more complex 3D architectures, such as triply periodic minimal surface-based porous bioceramics, have recently been explored to further optimize mechanical performance and bone ingrowth,[28,29] the present study intentionally adopted a simple orthogonally interconnected rectangular pore design with 500–800 µm channels to ensure reproducible fabrication and to achieve compressive strength exceeding 10 MPa for defect-site stabilization.

$$Porosity\left(\%\right)=1-\frac{\text{Bulk density}}{\text{Apparent density}}\times 100 \quad (1)$$

3.2. Radiographic evaluation of postoperative implant stability and early bone regeneration

Postoperative radiographs were used as a qualitative tool to assess implant positioning, defect alignment, and progressive mineralized tissue formation in both treatment groups. In the integrated Ti6Al4V plate–gradient-porous Ti6Al4V cage group (Figure 5), day 1 radiographs showed good alignment of the implant with the rabbit tibia, indicating satisfactory initial fixation. By day 90, increased radiopacity was observed around the defect region (yellow arrow), suggesting progressive mineralized tissue

formation and structural integration with the host bone. Because slight differences in limb positioning, anatomical orientation, and surgical handling were unavoidable across imaging sessions, direct comparison of radiographic contours between time points should be interpreted with caution. Accordingly, these X-ray images were primarily used for qualitative follow-up, whereas quantitative evaluation of bone regeneration was further performed using micro-CT and histological analyses.

The favorable radiographic appearance of the Ti6Al4V cage group may be related to its gradient-porous design, which incorporates a denser outer region to maintain mechanical support and a more porous inner architecture to facilitate tissue infiltration and vascularization. This design concept is consistent with previous reports showing that Ti6Al4V scaffolds with pore sizes of 500–600 μm and porosities of 60–70% provide a favorable balance between mechanical performance and osteogenesis.[30] Gu *et al.*[30] demonstrated that pore geometry significantly affects osteointegration outcomes in long-bone defect models, highlighting the importance of precise architectural control in translational scaffold design.

In the hybrid Ti6Al4V bone plate paired with an interconnected porous 3D bioceramic cage group (Figure 6), radiographs on day 1 also demonstrated satisfactory implant positioning and defect stabilization. At day 90, increased radiopacity within and around the defect region was more evident, consistent with enhanced bone ingrowth and mineralized tissue deposition. This finding is attributable to the osteoconductive nature of the interconnected β-TCP cage and its 500–800 μm pore channels, which facilitate cell migration, nutrient transport, and vascular invasion.[31] The bioceramic cage also served as a defect-guiding framework, promoting bone formation within the scaffold channels rather than complete restoration of the original cortical contour at this stage. Thus, the radiographic outcome suggests that the combined Ti6Al4V plate and porous bioceramic cage provided immediate mechanical fixation while supporting defect-directed bone regeneration. Although this configuration may help create a more favorable biological fixation environment at the bone–implant interface,[32] its regenerative effect should be interpreted in conjunction with micro-CT and histological findings rather than from radiographs alone. At this stage, successful repair should not be interpreted solely as the restoration of the original bone contour, but rather as the establishment of a stable, osteointegrated construct that supports progressive bridging of the defect.

3.3. *Ex vivo* micro-computed tomography evaluation after bone plate removal

Figure S3 shows 35 μm-resolution micro-CT images of the rabbit tibial defect region after implantation of either the FEA-optimized 3D-printed Ti6Al4V bone plate with a gradient-porous Ti6Al4V cage (Figure S3A) or the FEA-optimized 3D-printed Ti6Al4V bone plate combined with an interconnected porous 3D bioceramic cage (Figure S3B). In both configurations, severe metal artifacts from the Ti6Al4V bone plate substantially compromised image quality and prevented a reliable quantitative assessment of bone regeneration. In particular, the artifact was even more pronounced in the Ti6Al4V cage group because both the plate and cage were metallic. As a result, parameters such as BV within the defect, trabecular architecture, and scaffold degradation could not be accurately quantified from the in-situ scans alone. These observations indicate that alternative approaches, including histological analysis and *ex vivo* micro-CT after plate removal, are necessary for more reliable evaluation.

Figure 7 presents high-resolution *ex vivo* micro-CT images (9 μm) obtained 90 days after surgery from the Ti6Al4V bone plate paired with an interconnected porous 3D bioceramic cage group following plate removal. Sagittal (Figure 7A), coronal (Figure 7B), and axial (Figure 7C) views, together with the gross appearance after plate removal (Figure 7D), allowed distinction among host bone, newly formed bone, and residual calcium phosphate scaffold. Quantitative analysis showed that newly formed bone occupied 12 ± 1.4% of the defect volume. Although the amount of regenerated bone remained partial at this time point, the images clearly demonstrated bone ingrowth within and around the porous 3D bioceramic cage, while a substantial portion of the scaffold remained intact. This finding suggests that the calcium phosphate cage provided sustained structural support during the early repair stage while allowing progressive osteoconductive regeneration. Previous studies have emphasized that successful bone substitutes require a balance between scaffold degradation and new bone formation, since excessively rapid resorption may lead to loss of structural stability and impaired healing.[33-35] In this context, the interconnected 3D bioceramic cage appeared to provide a favorable balance between biological integration and mechanical support, supporting its potential utility for segmental bone defect repair. However, no metal artifact reduction algorithm was applied during micro-CT acquisition in this study. Quantitative morphometric analysis was therefore performed only after physical removal of the Ti6Al4V

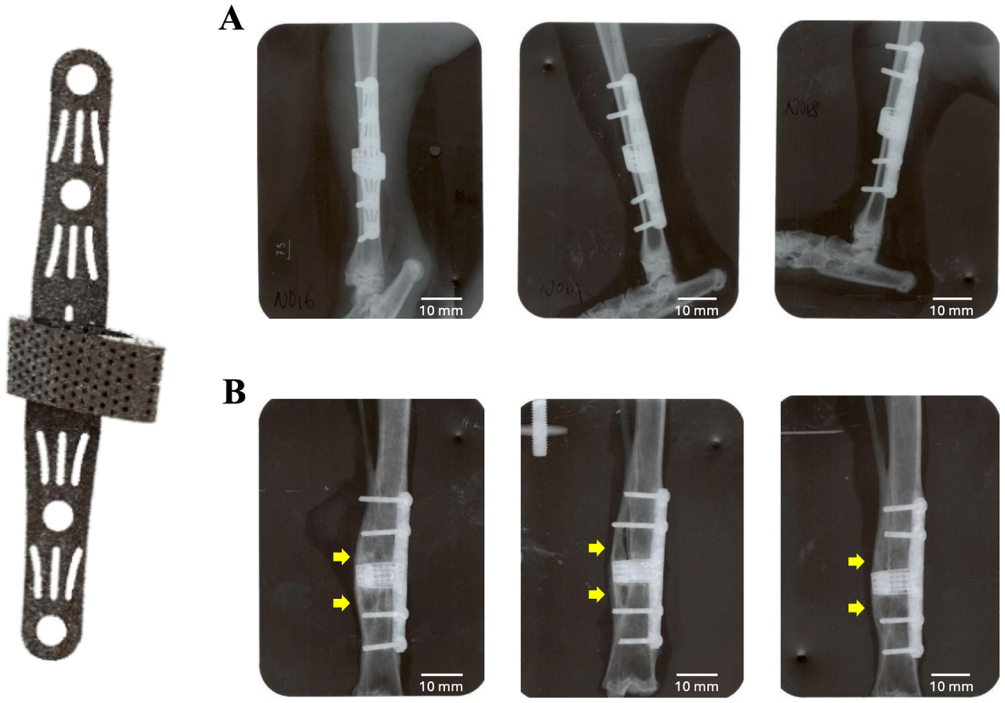

Figure 5. The optimal 3D Ti6Al4V-BP with a gradient-porous Ti6Al4V cage is used for tibia segment bone defect fixation after surgery. Three sets of experimental implants are shown at (A) 1 day and (B) 90 days after surgery, emphasizing their design for segmental bone defect fixation and stabilization, as illustrated by radiographic imaging. Scale bars: 10 mm; magnifications: 0.6×.

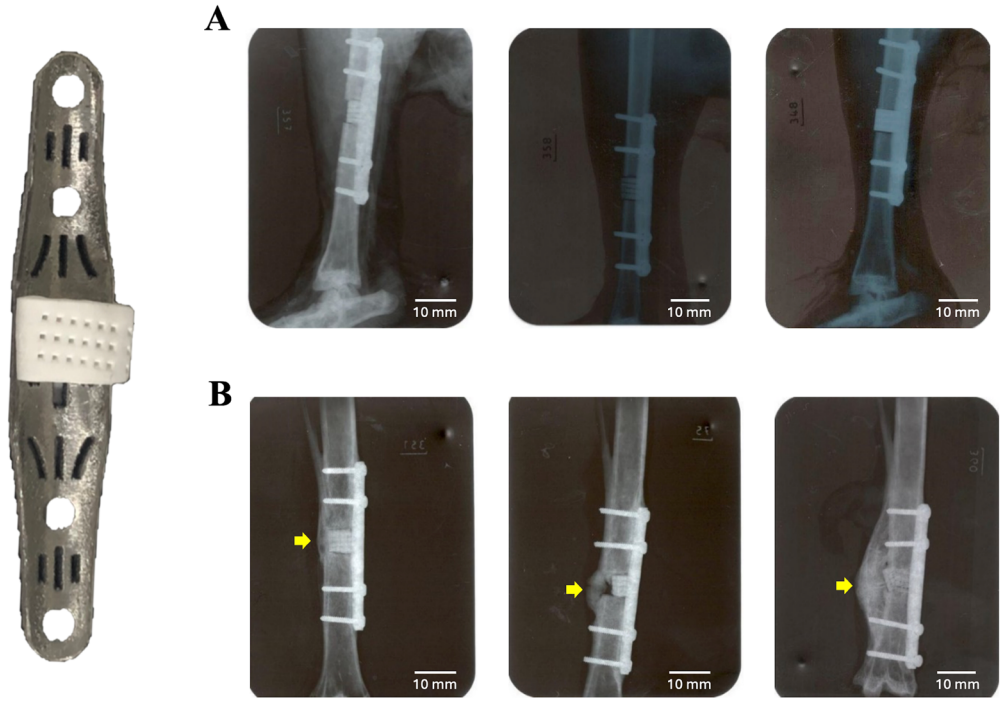

Figure 6. The optimized 3D Ti6Al4V-BP is paired with an interconnected porous 3D bioceramic cage used for tibia segment bone defect fixation after surgery. Three sets of experimental implants on (A) day 1 and (B) day 90 after surgery, emphasizing their design for segment bone defect fixation and stabilization, as illustrated by radiographic imaging (X-ray). Scale bars: 10 mm; magnifications: 0.6×.

plate, which, while effective in eliminating titanium-related artifacts, precluded in situ longitudinal assessment of bone formation beneath the intact construct.

On the other hand, quantitative micro-CT analysis was performed exclusively in the hybrid β-TCP cage group following plate removal, as metal artifacts precluded reliable morphometric assessment in the Ti6Al4V cage group. Accordingly, direct quantitative comparison between groups was not performed. The micro-CT findings for the hybrid group are therefore presented as descriptive, within-group observations, and should not be interpreted as evidence of superiority over the Ti6Al4V cage construct. The inability to obtain quantitative micro-CT morphometric data for the Ti6Al4V cage group due to metal artifacts represents a significant methodological limitation of the present study. Future investigations should consider the use of metal-artifact reduction algorithms and an alternative quantitative histomorphometric analysis of undecalcified sections technique to enable meaningful inter-group comparisons.

Ex vivo micro-CT imaging at the terminal timepoint demonstrated that the β-TCP cage remained structurally recognizable, suggesting that complete scaffold resorption had not occurred within the 90-day observation period. A separate *ex vivo* degradation assay further showed that β-TCP specimens immersed in PBS at 37 ± 1 °C underwent only 1.5% mass loss over 28 days (Figure S4), indicating slow β-TCP specimen dissolution under simplified physiological conditions. Nevertheless, because *in vivo* degradation is influenced by additional biological factors, such as osteoclastic activity, tissue infiltration, vascularization, and local ionic exchange, the *ex vivo* PBS data cannot be considered a direct measure of *in vivo* degradation kinetics. Rather, these findings should be interpreted as complementary evidence that the scaffold retained structural stability during the early repair stage. Quantitative assessment of *in vivo* degradation kinetics will require further longitudinal investigation.

3.4. Histological evaluation of tissue ingrowth and bone regeneration

Because the metallic Ti6Al4V cage was difficult to section directly, specimens from this group were decalcified first,

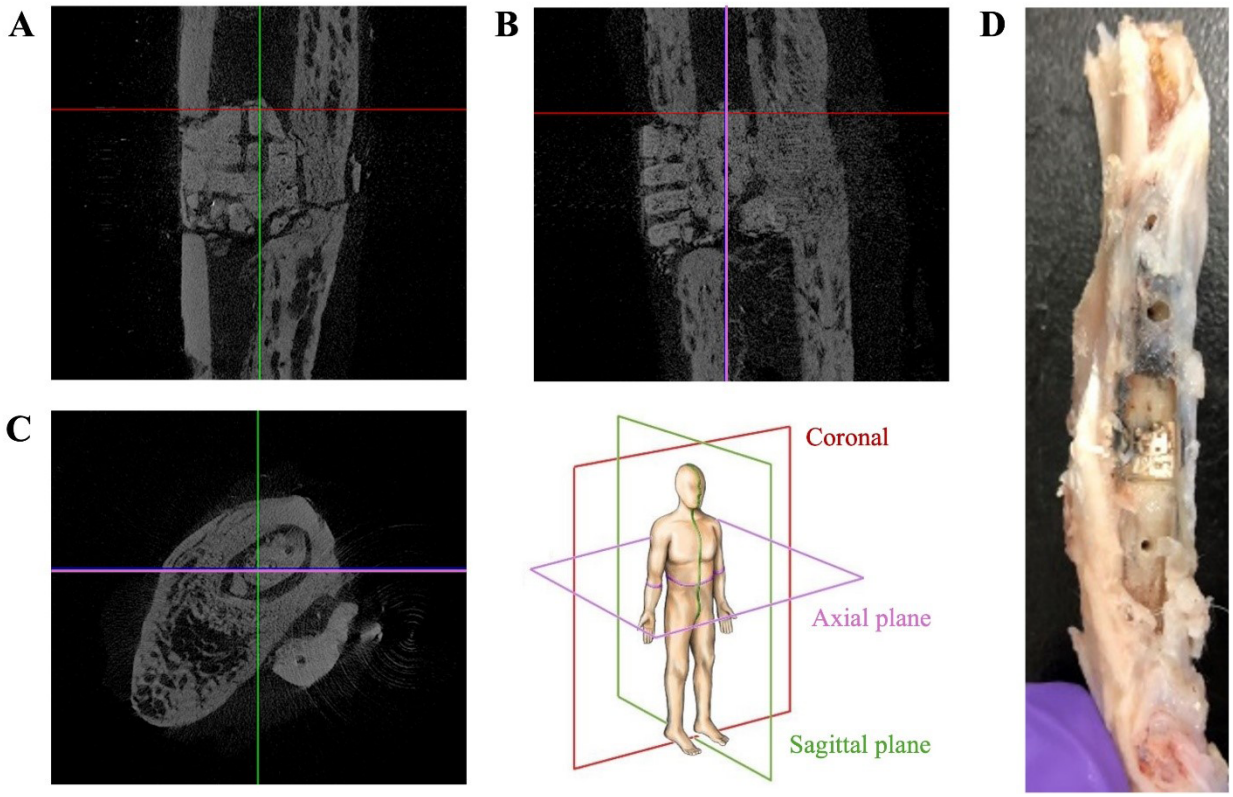

Figure 7. *Ex vivo* micro-computed tomography (CT) evaluation of rabbit tibial defects 90 days after implantation of the optimized 3D-printed Ti6Al4V bone plate (3D Ti6Al4V-BP) combined with an interconnected porous β-tricalcium phosphate bioceramic cage. After removal of the Ti6Al4V bone plate, high-resolution micro-CT imaging (9 μm) was performed to assess bone regeneration within the defect region. Representative cross-sectional images in the (A) sagittal, (B) coronal, and (C) axial planes, together with the (D) gross appearance of the tibial defect specimen after plate removal.

and the tissue ingrown within the cage was carefully retrieved before embedding and sectioning. Consequently, the exact spatial orientation of the histological sections could not be precisely defined; however, the analyzed tissue could still be confirmed to have originated from within the Ti alloy scaffold. Histological examination of the three specimens from the gradient-porous Ti6Al4V cage group (Figure 8) demonstrated tissue ingrowth within the internal scaffold architecture. H&E staining showed eosinophilic extracellular matrix and hematoxylin-stained nuclei, consistent with newly formed tissue occupying the porous structure. In several regions, cells morphologically consistent with osteoblast-like cells were observed lining matrix-rich areas within the scaffold, suggesting ongoing bone formation. In addition, fibrous connective tissue and small vascular structures were present, indicating soft tissue integration and angiogenic infiltration. These observations are consistent with previous reports showing that porous Ti-based scaffolds can support tissue migration, matrix deposition, and osteogenic repair.[36-38] However, because the sectioning approach disrupted the original scaffold–tissue spatial relationship, this group primarily provides qualitative evidence of tissue ingrowth rather than precise histomorphometric localization. Furthermore, as reported for gradient-porous Ti6Al4V scaffolds, pore architecture strongly influences the depth and uniformity of bone ingrowth, whereas residual stress shielding in denser regions may still affect long-term interfacial remodeling.[39,40]

In contrast, specimens from the FEA-optimized 3D-printed Ti6Al4V bone plate paired with an interconnected porous 3D bioceramic cage could be more readily detached from the Ti alloy plate after 90 days of decalcification, allowing for more reliable histological

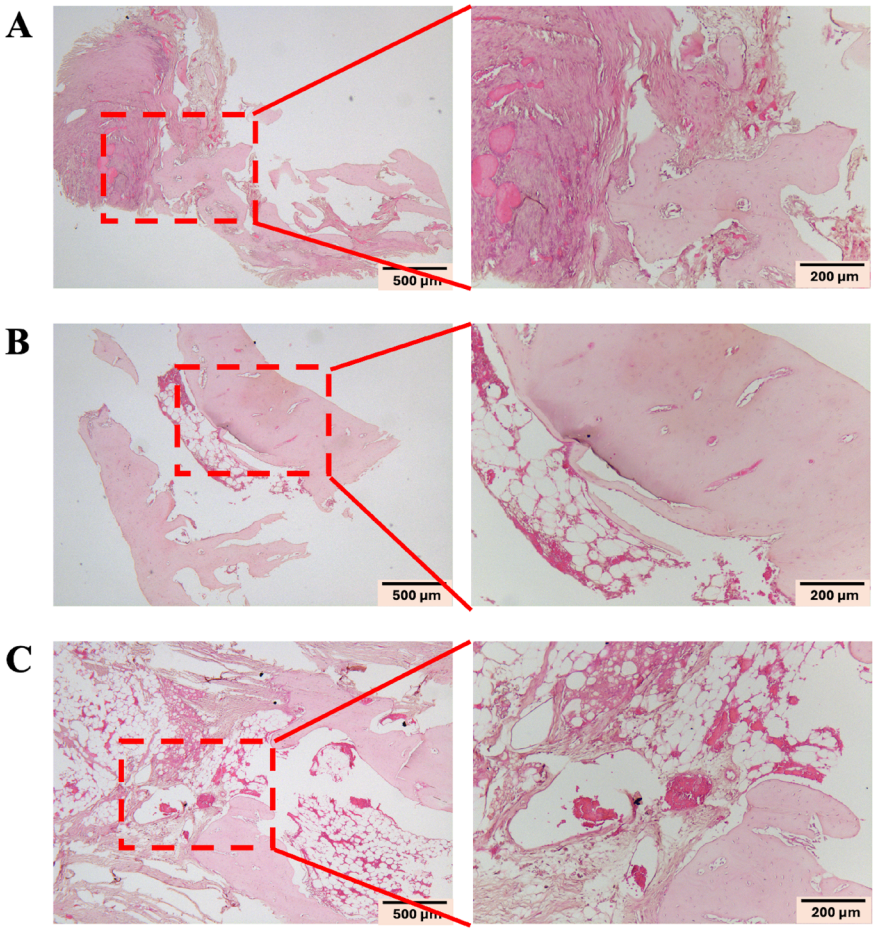

Figure 8. Hematoxylin and eosin-stained histological images of tissue retrieved from the gradient-porous Ti6Al4V cage group 90 days after implantation in the rabbit tibial segmental defects fixed with the finite element analysis-optimized 3D Ti6Al4V bone plate. Images from three representative animals are shown: (A) Sample 1, (B) Sample 2, and (C) Sample 3. Red dotted boxes indicate enlarged areas. Scale bars: (left panels) 500 μm, (right panels) 200 μm; magnifications: (left panels) 4×, (right panels) 10×.

evaluation (Figure S5). Histological images of all three specimens (Figure 9) and panoramic views (Figure S6) revealed substantial tissue infiltration and new bone formation within the porous bioceramic cage. Longitudinal H&E sections showed matrix-rich tissue extending from the host bone ends into the scaffold channels, with areas of trabecular-like new bone and cells morphologically consistent with osteoblast-like cells aligned along newly deposited matrix, indicating active osteogenic repair. Minimal multinucleated osteoclast-like cells were observed in these sections, suggesting that bone formation remained the predominant process at this stage.[41] Notably, the extent of defect bridging and matrix maturation varied among animals, with Sample 2 (Figure 9B) showing a more organized and mature trabecular-like structure than the other two specimens. Overall, these findings indicate that the Ti6Al4V bone plate maintained fixation stability, whereas the interconnected calcium phosphate cage

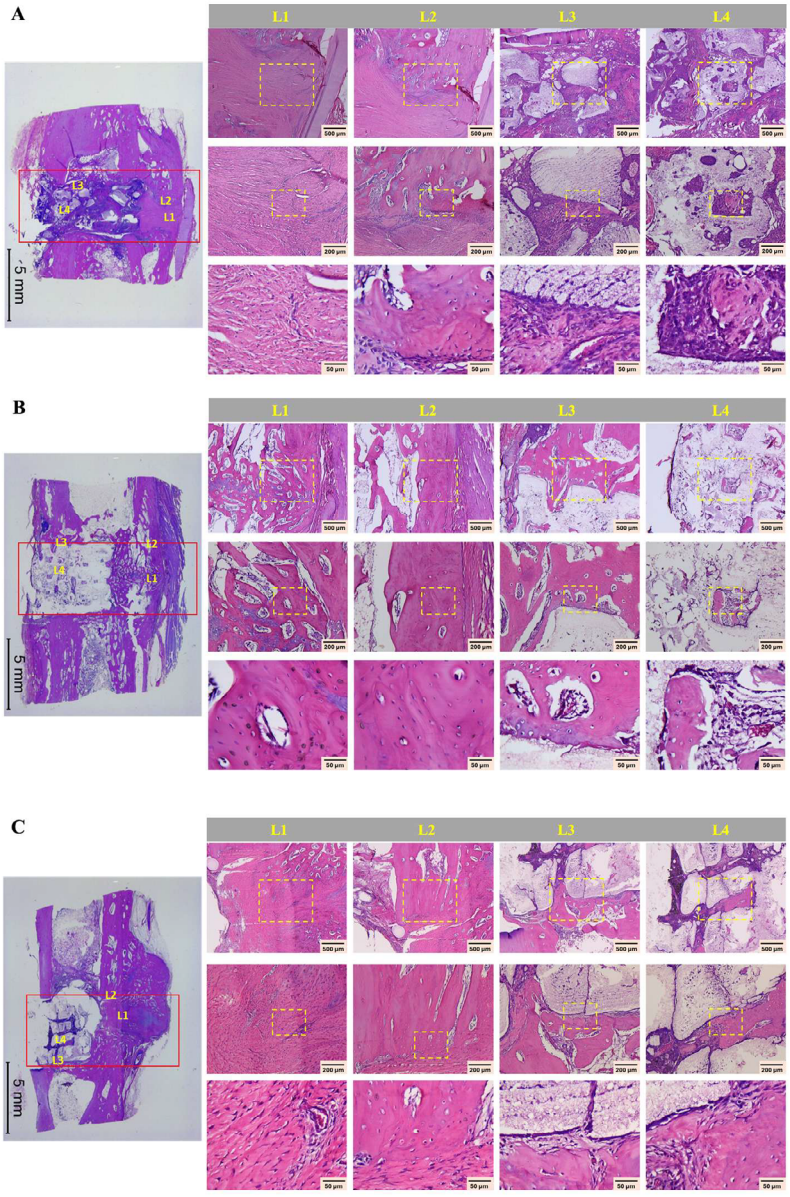

Figure 9. Hematoxylin and eosin-stained histological images of decalcified whole tibial defect specimens 90 days after implantation of the finite element analysis-optimized 3D Ti6Al4V bone plate paired with an interconnected 3D porous bioceramic cage in rabbit tibial segmental defects. Images from three representative animals are shown: (A) Sample 1, (B) Sample 2, and (C) Sample 3. L1–L4 indicate image locations within each specimen, and yellow dotted boxes indicate enlarged areas. Scale bars: (left panels) 5 mm, (first rows) 500 μm, (second rows) 200 μm, (third rows) 50 μm; magnifications: (left panels) 1×, (first rows) 4×, (second rows) 10×, (third rows) 40×.

provided an osteoconductive framework that supported progressive bone ingrowth and tissue integration.

The peripheral regions (L1 and L2) generally showed less organized repair tissue, including fibrous connective tissue, marrow-like spaces containing adipocyte-like cells, and early callus-like matrix, whereas the more central regions within the scaffold channels (L3 and L4) more frequently exhibited organized bone matrix and trabecular-like structures. For example, Sample 2 (L3 and L4) showed a denser and more structured matrix with osteoblast-like lining cells, consistent with more advanced ossification, whereas Sample 3 (L4) showed bone matrix associated with visible vascular structures, suggesting active vascularized tissue integration. Blood vessel-like structures were identified in several regions, supporting angiogenesis within the scaffold. Together, these findings suggest that the interconnected porous bioceramic cage supported a heterogeneous yet favorable healing microenvironment comprising bone-forming tissue, fibrous stroma, and vascular components, all of which are important for defect repair and long-term scaffold integration.[42-44] Although the degree of defect consolidation remained variable across specimens at 90 days, the overall histological pattern supports the osteoconductive and regenerative potential of the porous calcium phosphate cage in this segmental defect model.

Although both groups underwent the same decalcification protocol, the metallic nature of the Ti6Al4V cage necessitated manual retrieval of ingrown tissue prior to embedding, disrupting the original scaffold-tissue spatial relationship. This limited the histological assessment of bone ingrowth distribution and depth in the Ti6Al4V group relative to the intact β-TCP specimens. Future studies should consider alternative approaches such as resin-embedded ground-sectioning of metallic scaffolds without prior tissue retrieval, or micro-CT-guided virtual sectioning to reconstruct 3D ingrowth patterns non-destructively, enabling more valid inter-group histological comparisons.

4. Conclusion

This study presents a hybrid strategy for segmental bone defect reconstruction by combining a mechanically optimized 3D-printed Ti6Al4V bone plate with an osteoconductive interconnected porous 3D bioceramic cage. The Ti6Al4V bone plate, designed based on CT-derived anatomy and FEA, and fabricated by selective laser melting, incorporated a gradient-porous cage architecture (50–70%) intended to reduce stress concentrations and improve load transfer. Preliminary observations suggested that fixation with the bone plate alone was insufficient for maintaining stability in severe segmental defects, highlighting the need for an adjunctive regenerative scaffold. The bioceramic cage, fabricated by DLP using a negative thermo-responsive slurry system, developed into an interconnected porous structure with pore channels of 500–800 μm after sintering at 1,150 °C. The scaffold exhibited a porosity of 55.3%, while the ceramic struts remained highly densified, providing a favorable balance between structural support and biological permeability. XRD confirmed that the predominant crystalline phase after sintering was β-TCP. *In vivo* evaluation in a rabbit tibial segmental defect model demonstrated that both implant configurations provided immediate postoperative fixation. *Ex vivo* micro-CT revealed 12 ± 1.4% new bone formation within the defect region, and histological analysis demonstrated tissue infiltration, vascularization, and active bone formation within the scaffold. Collectively, these findings indicate that the Ti6Al4V bone plate provided essential early mechanical fixation, while the interconnected porous bioceramic cage supported osteoconductive healing and progressive defect repair. This hybrid fixation–regeneration strategy, therefore, shows promise for the treatment of segmental bone defects and warrants further validation in larger animal models, with potential translational relevance for long-bone reconstruction and high tibial osteotomy. Given the exploratory nature of this investigation, these findings should be regarded as hypothesis-generating rather than confirmatory. Future studies incorporating larger cohorts, formal statistical analysis, and appropriate control groups will be necessary to establish the clinical translational potential of this hybrid strategy.

Acknowledgments

We gratefully acknowledge the support and cooperation of the Orthopedic Research Center at Kaohsiung Medical University, Kaohsiung, with special thanks to Yi-Shan Lin for valuable contributions to this study. We also extend our appreciation to the members of the Department of Physiology at Kaohsiung Medical University, Kaohsiung, Taiwan. We recognize that the assistance provided was instrumental in achieving the results of this research and sincerely express our gratitude. We also thank the Center for Laboratory Animals at Kaohsiung Medical University for their support in animal care. Technical assistance with TGA data was kindly provided by the Thermal Analysis System of the Instrumentation Center, National Taiwan University. XRD (XRD000705) and SEM (EM001500) data were obtained from the High-Value Instrumentation Center, National Sun Yat-sen University.

Funding

This study was funded by the Ministry of Science and Technology of Taiwan (MOST 109-2314-B-037-135), the National Science and Technology Council of Taiwan (NSTC 110-2622-B-037-002, NSTC 112-2622-B-037-001, and NSTC 113-2314-B-037-024-MY2), and the Kaohsiung Medical University Research Center Grant (109KN004 and KMU-TC111A02-3).

Conflicts of interest

The authors declare they have no competing interests.

Author contributions

Conceptualization: Sung-Yen Lin, Chih-Yun Lee, Yen-Han Lai, Chung-Hwan Chen, Wen-Fan Chen, Cheng-Tang Pan, Yu-Shun Cheng, Chih-Kuang Wang
Formal analysis: Sung-Yen Lin, Chih-Yun Lee, Yen-Han Lai, Chung-Hwan Chen
Investigation: Chih-Kuang Wang
Methodology: Sung-Yen Lin, Chih-Yun Lee, Yen-Han Lai, Chung-Hwan Chen, Wen-Fan Chen, Cheng-Tang Pan, Yu-Shun Cheng
Resources: Chih-Kuang Wang
Supervision: Chih-Kuang Wang
Validation: Wen-Fan Chen, Cheng-Tang Pan, Yu-Shun Cheng
Visualization: Chih-Kuang Wang, Chih-Yun Lee
Writing–original draft: Sung-Yen Lin, Chih-Yun Lee, Yen-Han Lai, Chung-Hwan Chen
Writing–review & editing: Chih-Kuang Wang

Ethics approval and consent to participate

Ethics approval was obtained from the Institutional Animal Care and Use Committee of the Kaohsiung Medical University (KMU) Animal Research Center in Taiwan (Approval no. 108196).

Consent for publication

Not applicable.

Availability of data

Data are available from the corresponding author on reasonable request.

References

1. Grün W, Hansen EJJ, Andreassen GS, Clarke-Jenssen J, Madsen JE. Functional outcomes and health-related quality of life after reconstruction of segmental bone loss in femur and tibia using the induced membrane technique. *Arch Orthop Trauma Surg*. 2023;143(8):4587-4596.

   doi: 10.1007/s00402-022-04714-9

2. Konda SR, Gage M, Fisher N, Egol KA. Segmental bone defect treated with the induced membrane technique. *J Orthop Trauma*. 2017;31 Suppl 3:S21-S22.

   doi: 10.1097/BOT.0000000000000899

3. Moura LB, Carvalho PH de A, Xavier CB, *et al*. Autogenous non-vascularized bone graft in segmental mandibular reconstruction: a systematic review. *Int J Oral Maxillofac Surg*. 2016;45(11):1388-1394.

   doi: 10.1016/j.ijom.2016.05.004

4. Mohammadi SS, Phull SS, Bal BS, Towler MR. Bone void filler materials for augmentation in comminuted fractures: a comprehensive review. *J Orthop Surg Res*. 2025;20(1):449.

   doi: 10.1186/s13018-025-05857-2

5. Sumner DR. Long-term implant fixation and stress-shielding in total hip replacement. *J Biomech*. 2015;48(5):797-800.

   doi: 10.1016/j.jbiomech.2014.12.021

6. Qu H, Fu H, Han Z, Sun Y. Biomaterials for bone tissue engineering scaffolds: a review. *RSC Adv*. 2019;9(45):26252-26262.

   doi: 10.1039/c9ra05214c

7. Łuczak JW, Palusińska M, Matak D, *et al*. The future of bone repair: Emerging technologies and biomaterials in bone regeneration. *Int J Mol Sci*. 2024;25(23):12766.

   doi: 10.3390/ijms252312766

8. Marin E, Lanzutti A. Biomedical applications of titanium alloys: A comprehensive review. *Materials (Basel)*. 2023;17(1):114.

   doi: 10.3390/ma17010114

9. Dewidar M, Mohamed HF, Jae-Kyoo Lim. A new approach for manufacturing a high porosity Ti-6Al-4V scaffolds for biomedical applications. *J Mater Sci Technol*. 2008;24(6):931.

10. Wang R, Ni S, Ma L, Li M. Porous construction and surface modification of titanium-based materials for osteogenesis: A review. *Front Bioeng Biotechnol*. 2022;10:973297.

    doi: 10.3389/fbioe.2022.973297

11. Brochu BM, Sturm SR, Kawase De Queiroz Goncalves JA, *et al*. Advances in bioceramics for bone regeneration: A narrative review. *Biomimetics (Basel)*. 2024;9(11):690.

    doi: 10.3390/biomimetics9110690

12. Lin CW, Su YF, Lee CY, *et al*. 3D printed bioceramics fabricated using negative thermoresponsive hydrogels and silicone oil sealing to promote bone formation in calvarial defects. *Ceram Int*. 2021;47(4):5464-5476.

    doi: 10.1016/j.ceramint.2020.10.129

13. Lee CY, Nedunchezian S, Lin SY, *et al*. Bilayer osteochondral graft in rabbit xenogeneic transplantation model comprising

sintered 3D-printed bioceramic and human adipose-derived stem cells laden biohydrogel. *J Biol Eng*. 2023;17(1):74.

doi: 10.1186/s13036-023-00389-x

14. Fu YC, Chen CH, Wang CZ, *et al*. Preparation of porous bioceramics using reverse thermo-responsive hydrogels in combination with rhBMP-2 carriers: in vitro and in vivo evaluation. *J Mech Behav Biomed Mater*. 2013;27:64-76.

doi: 10.1016/j.jmbbm.2013.06.009

15. Bose S, Vahabzadeh S, Bandyopadhyay A. Bone tissue engineering using 3D printing. *Mater Today (Kidlington)*. 2013;16(12):496-504.

doi: 10.1016/j.mattod.2013.11.017

16. Pan CT, Hsu WH, Cheng YS, Wen ZH, Chen WF. A new design of porosity gradient Ti-6Al-4V encapsulated hydroxyapatite dual materials composite scaffold for bone defects. *Micromachines (Basel)*. 2021;12(11):1294.

doi: 10.3390/mi12111294

17. Miltenberg B, Puzzitiello RN, Ruelos VCB, *et al*. Incidence of complications and revision surgery after high tibial osteotomy: A systematic review. *Am J Sports Med*. 2024;52(1):258-268.

doi: 10.1177/03635465221142868

18. Nguyen LH, Annabi N, Nikkhah M, *et al*. Vascularized bone tissue engineering: approaches for potential improvement. *Tissue Eng Part B Rev*. 2012;18(5):363-382.

doi: 10.1089/ten.TEB.2012.0012

19. Shi F, Xiao D, Zhang C, Zhi W, Liu Y, Weng J. The effect of macropore size of hydroxyapatite scaffold on the osteogenic differentiation of bone mesenchymal stem cells under perfusion culture. *Regen Biomater*. 2021;8(6):rbab050.

doi: 10.1093/rb/rbab050

20. Bacakova L, Filova E, Parizek M, Ruml T, Svorcik V. Modulation of cell adhesion, proliferation and differentiation on materials designed for body implants. *Biotechnol Adv*. 2011;29(6):739-767.

doi: 10.1016/j.biotechadv.2011.06.004

21. Zhou H, Lee J. Nanoscale hydroxyapatite particles for bone tissue engineering. *Acta Biomater*. 2011;7(7):2769-2781.

doi: 10.1016/j.actbio.2011.03.019

22. Habibovic P, Yuan H, van der Valk CM, Meijer G, van Blitterswijk CA, de Groot K. 3D microenvironment as essential element for osteoinduction by biomaterials. *Biomaterials*. 2005;26(17):3565-3575.

doi: 10.1016/j.biomaterials.2004.09.056

23. Wang X, Nie Z, Chang J, Lu ML, Kang Y. Multiple channels with interconnected pores in a bioceramic scaffold promote bone tissue formation. *Sci Rep*. 2021;11(1):20447.

doi: 10.1038/s41598-021-00024-z

24. Park JY, Jung YN, Jang KJ, *et al*. Effect of axis change on shrinkage rate of 3D-printed bioceramic Zirconia fabricated via digital light processing. *Biomimetics (Basel)*. 2025;10(3):140.

doi: 10.3390/biomimetics10030140

25. Hussain M, Xia M, Ren X, *et al*. Digital light processing 3D printing of ceramic materials: a review on basic concept, challenges, and applications. *Int J Adv Manuf Technol*. 2024;130:2241-2267.

doi: 10.1007/s00170-023-12847-3

26. Sim JH, Koo BK, Jung M, Kim DS. Study on debinding and sintering processes for ceramics fabricated using digital light processing (DLP) 3D printing. *Processes (Basel)*. 2022;10(11):2467.

doi: 10.3390/pr10112467

27. Barzanouni H, Houreh AB, Solati-Hashjin M, Barzanouni A, Shafieian M. 3D-Printed PLA: β-TCP scaffolds: fabrication and evaluation for bone regeneration in load-bearing defects. *Polym Adv Technol*. 2025;36(12):e70466.

doi: 10.1002/pat.70466

28. Guo W, Li P, Pang Y, *et al*. Biomimetic TPMS porous hydroxyapatite bone scaffolds doped with bioactive glass: digital light processing additive manufacturing, microstructure and performance. *Compos Part A Appl Sci Manuf*. 2025;193:108870.

doi: 10.1016/j.compositesa.2025.108870

29. Li Y, Li J, Jiang S, *et al*. The design of strut/TPMS-based pore geometries in bioceramic scaffolds guiding osteogenesis and angiogenesis in bone regeneration. *Mater Today Bio*. 2023;20:100667.

doi: 10.1016/j.mtbio.2023.100667

30. Gu Y, Sun Y, Shujaat S, Braem A, Politis C, Jacobs R. 3D-printed porous Ti6Al4V scaffolds for long bone repair in animal models: a systematic review. *J Orthop Surg Res*. 2022;17(1):68.

doi: 10.1186/s13018-022-02960-6

31. Wang X, Lin M, Kang Y. Engineering porous β-tricalcium phosphate (β-TCP) scaffolds with multiple channels to promote cell migration, proliferation, and angiogenesis. *ACS Appl Mater Interfaces*. 2019;11(9):9223-9232.

doi: 10.1021/acsami.8b22041

32. Ducheyne P, Bianco PD, Kim C. Bone tissue growth enhancement by calcium phosphate coatings on porous titanium alloys: the effect of shielding metal dissolution product. *Biomaterials*. 1992;13(9):617-624.

doi: 10.1016/0142-9612(92)90030-r

33. Lutzweiler G, Ndreu Halili A, Engin Vrana N. The overview of porous, bioactive scaffolds as instructive biomaterials for tissue regeneration and their clinical

translation. *Pharmaceutics*. 2020;12(7):602.

doi: 10.3390/pharmaceutics12070602

34. Ivanovski S, Breik O, Carluccio D, Alayan J, Staples R, Vaquette C. 3D printing for bone regeneration: challenges and opportunities for achieving predictability. *Periodontol 2000*. 2023;93(1):358-384.

doi: 10.1111/prd.12525

35. Sadat-Shojai M, Asadnia M, Shahsavani MB, Yousefi MM. Bone regenerative medicine: An emerging field with opportunities and challenges. *J Am Ceram Soc*. 2025;108(11):e20508.

doi: 10.1111/jace.20508

36. Yuan B, Liu P, Zhao R, *et al*. Functionalized 3D-printed porous titanium scaffold induces in situ vascularized bone regeneration by orchestrating bone microenvironment. *J Mater Sci Technol*. 2023;153:92-105.

doi: 10.1016/j.jmst.2022.12.033

37. Liu J, Jin F, Zheng ML, *et al*. Cell behavior on 3D Ti-6Al-4V scaffolds with different porosities. *ACS Appl Bio Mater*. 2019;2(2):697-703.

doi: 10.1021/acsabm.8b00550

38. Ma L, Wang X, Zhou Y, *et al*. Biomimetic Ti-6Al-4V alloy/gelatin methacrylate hybrid scaffold with enhanced osteogenic and angiogenic capabilities for large bone defect restoration. *Bioact Mater*. 2021;6(10):3437-3448.

doi: 10.1016/j.bioactmat.2021.03.010

39. Van Bael S, Chai YC, Truscello S, *et al*. The effect of pore geometry on the in vitro biological behavior of human periosteum-derived cells seeded on selective laser-melted Ti6Al4V bone scaffolds. *Acta Biomater*. 2012;8(7):2824-2834.

doi: 10.1016/j.actbio.2012.04.001

40. Arabnejad S, Johnston B, Tanzer M, Pasini D. Fully porous 3D printed titanium femoral stem to reduce stress-shielding following total hip arthroplasty. *J Orthop Res*. 2017;35(8):1774-1783.

doi: 10.1002/jor.23445

41. LeGeros RZ. Properties of osteoconductive biomaterials: calcium phosphates. *Clin Orthop Relat Res*. 2002;395(395):81-98.

doi: 10.1097/00003086-200202000-00009

42. Hutmacher DW. Scaffolds in tissue engineering bone and cartilage. *Biomaterials*. 2000;21(24):2529-2543.

doi: 10.1016/s0142-9612(00)00121-6

43. Bose S, Roy M, Bandyopadhyay A. Recent advances in bone tissue engineering scaffolds. *Trends Biotechnol*. 2012;30(10):546-554.

doi: 10.1016/j.tibtech.2012.07.005

44. Wong SK, Yee MMF, Chin KY, Ima-Nirwana S. A review of the application of natural and synthetic scaffolds in bone regeneration. *J Funct Biomater*. 2023;14(5):286.

doi: 10.3390/jfb14050286